

# A study of a coronal hole associated with a large filament eruption

Heidy Gutiérrez,<sup>1</sup>★ Lela Taliashvili,<sup>1</sup> Alexandre Lazarian<sup>2</sup> and Zadig Mouradian<sup>3</sup>

<sup>1</sup>*Space Research Center (CINESPA), School of Physics, University of Costa Rica, 2060 San José, Costa Rica*

<sup>2</sup>*Department of Astronomy, University of Wisconsin, 475 North Charter Street, Madison, WI 53706, USA*

<sup>3</sup>*LESIA–UMR 8100–Observatoire de Paris, CNRS, Univ. Paris 6&7, F-92190 Meudon, France*

Accepted 2017 July 19. Received 2017 July 19; in original form 2017 February 6

## ABSTRACT

We report the results of a detailed study of an equatorial coronal hole and a dimming region related to the eruptions of a nearby large filament and subsequent coronal mass ejections (CMEs). The dynamic eruptions of the filament and the associated CMEs are probably related to the magnetic reconnection involving the magnetic field lines at the filament footpoints. During the starting processes of the filament eruption, we observed several newly emerged small magnetic flux concentrations close to the filament footpoints. Disturbance increase in the prominence body was observed during the pre-eruption processes. After the filament eruption, we observed evacuated filament material from the filament channel towards the coronal hole. Thus, all the region is perturbed and EUV loops and bright points are observed before and after the eruptions. Additionally, after the CME, we observed the disappearance of the dimming region and the coronal hole, followed by photospheric magnetic diffusion. We discussed a possible magnetic reconnection scenario and MHD waves involved during these processes.

**Key words:** Sun: chromosphere – Sun: corona – Sun: coronal mass ejections (CMEs) – Sun: filaments, prominences – Sun: oscillations.

## 1 INTRODUCTION

The energetic evolution of solar prominences is characterized by the dynamic (DBd) or thermal (DBt) ‘disparition brusque’ of the prominence plasma (Tandberg-Hanssen 1995). DBds are believed to be associated with magnetic reconnection of the supporting magnetic field that leads to material ejection and acceleration of electrons in the high corona (Raadu et al. 1988). DBts, on the other hand, are caused by the heating of the prominence plasma followed by their disappearance in spectral lines with low formation temperature and subsequent appearance in lines with higher formation temperatures (Mouradian, Martres & Soru-Escaut 1980, 1986).

Coronal holes (CHs) are low-density and low-temperature coronal regions (Waldmeier 1975). They are predominantly magnetically unipolar areas, where the magnetic field extends outwards to form the interplanetary magnetic field and plasma escapes to form the solar wind (Krieger, Timothy & Roelof 1973; Cranmer 2002; Wang 2009). Dimming regions (DRs) are often referred to as transient CHs due to their similar dark appearance in EUV and X-ray wavelengths (Rust 1983; Kahler & Hudson 2001) and are characterized by open magnetic fluxes (Krista & Reinard 2013). DRs, which typically form in less than 1 h and slowly fade in 1–2 d, are relatively common events during CMEs and are also associated with filament eruptions, flares and coronal wave transients (de Toma et al. 2005, and references therein). A density decrease or a

temperature variation of the emitting plasma can cause a decrease in coronal brightness, but the rapid appearance of dimmings suggests that they occur due to density depletions (Hudson, Acton & Freeland 1996). In turn, a density depletion above the dimming regions could be caused by the ejection of coronal plasma along field lines opened during the CME or by a fast expansion of the plasma volume above the dimming regions (Gibson & Low 2000; Attrill et al. 2006).

CH topological changes associated with filament eruptions and subsequent formation of CMEs are related to magnetic reconnection as discussed in a number of studies (Bravo 1995; Gopalswamy et al. 2006; Jiang et al. 2007). Taliashvili, Mouradian & Páez (2009) found that when the distance between a CH boundary and a filament channel is within 15°, there is a relationship between the onset of a DBt and/or a DBd accompanied by a topological change of the CH, including the fading of the CH and the subsequent formation of a CME. Moreover, they found a direct relationship between the DBt near the faded CH and the formation of a low-speed, narrow CME. Madjarska, Doyle & van Driel-Gesztelyi (2004) reported the appearance/disappearance of EUV bright points as a direct observational evidence of magnetic reconnection at the boundaries of CH, causing short-term topological changes of CHs. Additionally, Gutiérrez, Taliashvili & Mouradian (2013) reported the appearance and disappearance of bright points close to the boundary of CHs as an evidence of magnetic reconnection followed by DBd of a nearby filament.

The physical process of transporting energy and heating the solar atmosphere, as well as accelerating the solar wind, has been

★ E-mail: [heidyt.gutierrez@cinespa.ucr.ac.cr](mailto:heidyt.gutierrez@cinespa.ucr.ac.cr)

associated with many authors (e.g. Hollweg 1981; Cranmer & van Ballegoijen 2005; Murawski et al. 2015) using MHD waves and turbulence. Alfvénic perturbations, as they interact non-linearly, introduce turbulence cascade (e.g. see Brandenburg & Lazarian 2013 for a review). The MHD perturbations as they interact can establish cascades with energy moving from large scale to small scales with dissipation taking place only at the smallest scales where either viscosity or various plasma microscale phenomena get importance. Depending on the strength of non-linear interactions, the MHD motions can stay oscillatory or decay significantly over a single period. The former corresponds, for instance, to the weak Alfvénic turbulence and the latter to the strong Alfvénic turbulence (e.g. see Brandenburg & Lazarian 2013, for a review). Sinusoidal Alfvén waves sent through turbulent media are also subject to non-linear decay (Yan & Lazarian 2002; Farmer & Goldreich 2004; Beresnyak & Lazarian 2007).

Magnetic turbulence can significantly enhance the reconnection rates (Lazarian & Vishniac 1999; Kowal et al. 2009; Sych et al. 2009; Eyink, Lazarian & Vishniac 2011). Magnetic reconnection is associated with the release of stored magnetic energy as waves and turbulence, bulk mechanical acceleration of material and heat. Moreover, the generation of turbulence by reconnection is also a part of turbulent reconnection models (Lazarian & Vishniac 1999; Lazarian, Vishniac & Kowal 2009; Beresnyak 2013; Lazarian et al. 2015).

We studied an equatorial CH and DR related to the nearby (located within  $15^\circ$  distance), large quiescent filament/prominence eruptions and associated CMEs during Carrington rotations (CRs) 2126 and 2127. The starting processes of filament instabilities are related to the increase of the whole filament body disturbances and newly emerging small magnetic fluxes close to the channel and footpoints of the filament. Several EUV loops and bright points formed before and after the filament eruptions. During the post-filament eruption and post-CME evolution phases, we observed strong perturbations of the region between the filament channel and the CH boundary. These perturbations are principally related to the evacuated filament's material motions and low coronal MHD waves that are propagating almost longitudinally along arcades over the filament channel towards the boundary of the CH. We also observed photospheric magnetic diffusion that started after the wave and turbulence dissipation, and the fading of the DR and the CH. We discussed possible magnetic reconnection during eruptions and CMEs in the perspective of the turbulence magnetic reconnection theory of Lazarian.

## 2 DATA SETS AND WORKING METHOD

We selected one long-lived quiescent equatorial filament and nearby CH and DR, located within  $15^\circ$  distance from the filament channel and studied their evolution and the associated CMEs during approximately 1 month (2012 August 3–September 5). For this detailed study, we analysed the evolution of the filament registered in  $H\alpha$  and EUV images. We used  $H\alpha$  images taken by Paris Observatory (PO) at Meudon and Global Oscillation Network Group (GONG). The PO  $H\alpha$  spectroheliograms that we used are calibrated and have a spatial resolution of  $4 \text{ arcsec pixel}^{-1}$ . The GONG images are calibrated and have a cadence of 20 s and a spatial resolution of  $1.052 \text{ arcsec pixel}^{-1}$ .

We also used EUV observations to study the evolution of CH and DR related to the filament instabilities based on images obtained by the Atmospheric Imaging Assembly (AIA; Lemen et al. 2012) aboard Solar Dynamics Observatory (SDO; Pesnell, Thompson & Chamberlin 2012) with the 304, 171, 193 and 211 Å

filters and the Extreme UltraViolet Imager (EUVI) of Sun Earth Connection Coronal and Heliospheric Investigation (SECCHI; Howard et al. 2008) aboard Solar TERrestrial Relations Observatory (STEREO; Kaiser 2005) with the 304 and 195 Å filters. The SDO/AIA images have a cadence of 12 s and a spatial resolution of  $0.6 \text{ arcsec pixel}^{-1}$ . The STEREO/EUVI images have a cadence of  $>2 \text{ min}$  and a spatial resolution of  $1.6 \text{ arcsec pixel}^{-1}$ . These images were calibrated and processed by the SDO and STEREO routines of Solar Software (SSW; `aia_prep.pro` and `euvi_prep.pro`).

To find the relationship between the eruption of the filament (or filament sections) and a CME(s), we considered the starting times, position angles and widths of the erupting filament (or filament sections) and CMEs based on the CME catalogues and images/movies reported by the Large Angle Spectroscopic Coronagraph (LASCO; Brueckner et al. 1995) aboard Solar and Heliospheric Observatory (SOHO; Domingo, Fleck & Poland 1995) and the coronagraphs (COR1 and COR2) of SECCHI onboard STEREO.

Finally, in order to study the magnetic evolution of the filament, CH, DR and their surroundings associated with the filament instabilities, we analysed the magnetograms provided by the Helioseismic and Magnetic Imager (HMI; Schou et al. 2012) onboard SDO and synoptic maps of the photospheric magnetic field from the Wilcox Solar Observatory (WSO; Scherrer et al. 1977; Duvall et al. 1977). The SDO/HMI provides longitudinal (or line-of-sight) magnetograms, with a cadence of 45 s and a spatial resolution of  $0.5 \text{ arcsec pixel}^{-1}$ , calibrated and processed by `hmi_prep.pro` (SSW).

## 3 DATA ANALYSIS AND DISCUSSION

### 3.1 Long-term evolution

The equatorial CH (of predominantly negative polarity), situated within  $15^\circ$  from the long-lived equatorial ( $\sim 45^\circ$  length) filament, started forming on 2012 August 3 (CR 2126). This filament has an additional northern unstable  $\sim 15^\circ$  length section, which can be observed mostly in the EUV images. Between them, almost parallel to the filament channel, extends a DR. Additionally, four small ARs surround the southern footpoint of the filament (Fig. 1). This filament is characterized by different evolutionary stages that we have discussed previously (Taliashvili et al. 2014). Let us summarize some important observations. Every evolutionary stage of this filament successively involved three sections that compose the filament's body: southern, central and northern, each of them characterized by a different evolution as usual (Mouradian & Soru-Escaut 1989). We observed independent, almost constant motion of the filament plasma within each of these sections, which would sometimes rise up. However, the whole filament remained visible until August 8. During the evolution of this filament, some additional peculiar instabilities were observed on August 4, 6, 7 and 25 in the form of the filament plasma arcing from the southern to the extreme northern footpoint and then subsequently returning to its original position along the same path. This extreme northern footpoint, which is clearly visible mostly in EUV images, is located at almost the same coordinates of the small magnetic flux (inside the circle in Fig. 1). These motions were preceded by the successive appearance of several new magnetic fluxes close to and along the channel and footpoints of filament. Moreover, C1.1–C3.5 flares, related to NOAA ARs 11539, 11540 and 11541, were observed 0.5–3 h before these motions. Thus, the filament plasma was launched from the southern towards the northern footpoint, following the same path of emerged fluxes and returned to its original

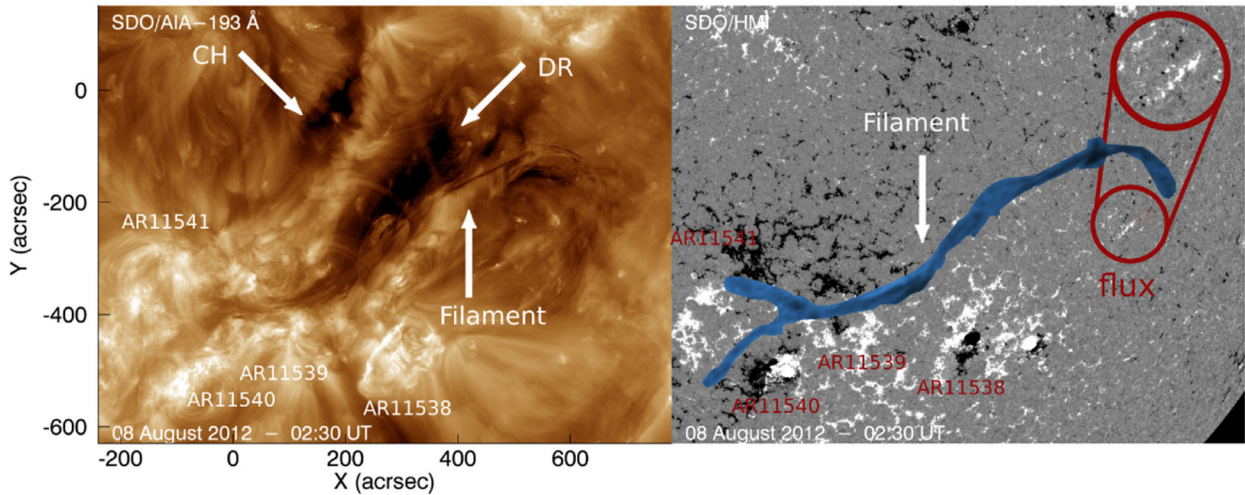


**Figure 1.** Left: SDO/AIA 193 Å image of 2012 August 8, 02:30 UT. The white arrows indicate the CH, DR, filament and four small ARs (11538, 11539, 11540 and 11541) near them. Right: SDO/HMI magnetograms for 2012 August 8, 02:30 UT, calibrated for  $\pm 80$  G. The filament is superimposed in blue colour, and it was taken from the GONG/H $\alpha$  image corresponding to the same observational time. The red circles indicate the small flux in original size and its zoom (adapted from Taliashvili, Mouradian & Gutiérrez 2014).

position. Each of these peculiar motions observed on August 4, 6 and 7 is followed by one of these three scenarios: (1) A small EUV loop connects to the southern footpoint of the filament, followed by the thermal disappearance of the southern section and a magnetic flux cancellation close to the southern footpoint, and then the loop moves radially from the cancelled flux and associated two narrow CMEs start accompanied by the growing of the filament and the CH. (2) A small transient CH forms within DR related to the evacuated filament plasma, followed by the growing of transient CH and the thermal disappearance of southern and central sections. (3) Dynamic eruptions of the northern section and the major part of the central section of the filament, accompanied by two consecutive CMEs, the perturbation of the region between the filament channel and CH and the disappearance of CH. Finally, on August 13, the southern section of the prominence and the remnant of the central section also erupted and were followed by consecutive CMEs. Based on STEREO/EUV evolution, the filament rebuilt as it is commonly observed (Mouradian et al. 1987) on August 14 and kept almost the same form. An additional peculiar instability of the filament started on August 25 near the central meridian (observed by STEREO-B) and on the West limb (observed by STEREO-A). Thus, after these motions, the filament always returned to its original position, keeping its shape, i.e. the magnetic field structure. Fig. 3 shows one of the newly emerged magnetic fluxes and its cancellation; this process was always followed by the filament thermal disappearance or/and eruption and CMEs. Lately, on August 30 (CR 20127) the filament was observed again from Earth with a CH on the eastern side of the filament (within  $15^\circ$  distance). The whole filament eruption started on August 31, accompanied by a Halo CME. Additionally, a new small equatorial transient CH formed within DR on the eastern side of the filament few hours before this eruption, which grew during the eruption and disappeared slowly after 3.5 d.

In this study, we focused on filament partial eruptions occurred on August 8, 03:45 UT, and the complete filament eruption on August 31, 17:00 UT (see Table 1).

### 3.2 Events of August 8, 2012: dynamics of the edge of a CH

We analysed the observations by SDO/AIA, PO and GONG that indicate the onset of eruptions of central and northern sections of

the filament on August 8, 03:45 UT, which occurred almost simultaneously with the flux cancellation (Fig. 3). These partial filament eruptions started after the filament plasma had flown from its southern footpoint towards the extreme northern footpoint and vice versa, as mentioned above, during the period of August 7, 23:01 UT–August 8, 03:00 UT (Fig. 3). During this filament plasma flow, we observed the additional plasma motion between the AR 11539 and the southern section. Also two small flares, C1.7-AR 11540 and C1.1-AR 11541, located close to the southern footpoint started 3 h before and 10 min after the starting time of eruptions, respectively. About 30 min after the starting time of eruptions, two consecutive West-limb CME1 and CME2 started at nearly identical position angles with respect to the central and northern sections (see Fig. 2 and Table 1).

SDO/AIA 211 and 193 Å observations show a series of coronal loops that formed at the heated region between the filament channel and the CH boundary before and after the partial eruptions (Fig. 4). Some loops are observed almost simultaneously with the filament plasma flow from its southern to the extreme northern footpoint on August 7 and some loops just before the onset of eruptions. Before and after the formation of these loops, several EUV bright points associated with the small magnetic dipoles appeared and disappeared quickly between the DR and the CH and very close to the filament channel and its southern footpoint. As observed in SDO/AIA 304 Å images (black arrows, Fig. 4), the loop formation was accompanied by the plasma motion from the filament channel to the western boundary of CH. Initially, just a few minutes before the eruptions, the filament plasma, related to a part of the central section not involved in filament eruption, moved from the central part of the filament channel, reached the western boundary of CH and induced the onset of CH fading (August 8, 07:15 UT; Fig. 4). Later, after the filament partial eruptions and CMEs, several additional loops formed and the evacuated filament plasma moved from the southern part of the filament channel, reached the southern side of CH and led to the disappearance of the dimming region and almost the whole CH (at 20:00 UT). Furthermore, the analysis of SDO/HMI magnetograms after the partial filament eruptions and the disappearance of DR and CH show the magnetic diffusion at the north side of the erupted northern section of the filament.

**Table 1.** Summary of key instabilities of the filament and associated activities during the period of 2012 August 7–September 4.

Activity	Date/Observations
The filament plasma arcing from the southern to the northern footpoint and then returning along the same path.	August 7, 23:01 –August 8, 03:00 UT (Fig. 3)
Several EUV loops formed between the filament channel and the western boundary of the CH.	August 7, 23:01 UT–August 8, 03:45 UT (Fig. 4)
DBd of CS and NS sections and the flux disappearance.	August 8, 03:45 UT (Fig. 3)
C1.7 (AR 11540) and C1.1 (AR 11541) flares.	August 8, ~00:45 UT and ~03:55 UT respectively
CME1: PA $\sim 255^\circ$ , W $\sim 20^\circ$ .	August 8, ~04:12 UT (Fig. 2)
Several EUV loops formed between the filament channel and the western boundary of CH.	From August 8, ~04:40 UT (Fig. 3)
CME2: PA $\sim 275^\circ$ , W $\sim 60^\circ$ .	August 8, ~05:48 UT (Fig. 2)
Plasma motions from the filament channel towards the CH.	August 8, 03:20 UT–11:00 UT (Fig. 4)
Disappearance of DR and CH.	August 8, 07:15 UT–20:00 UT (Fig. 4)
DBd of the SS and the CS's remnant, followed by two West-limb CMEs PA $\sim 259^\circ$ and W $\sim 53^\circ$ ; PA $\sim 255^\circ$ and W $\sim 27^\circ$	August 13, 09:36, 10:48, 13:25 UT, respectively
Prominence is reformed.	From August 14
The filament plasma arcing from the southern to the northern footpoint, and then subsequently returning along the same path.	August 25, 06:30 UT (on the far side of the Sun, observed by STEREO-B at the central meridian and by STEREO-A at the West limb)
The filament close to the CH and DR.	August 30, CR 2127 (Fig. 10)
The prominence expansion starting slowly.	August 31, ~17:00 UT
Complete DBd of prominence.	August 31, ~19:45 UT (Fig. 10)
C8.4 flare (AR 11563) and type II radio burst.	August 31, ~20:10 UT
Halo CME3.	August 31, ~20:10 UT (Fig. 9)
Formation of post-DBd/flare loops.	August 31, ~20:50 UT (Fig. 10)
Formation of post-CME loops.	September 1, 23:00 UT–September 3, 16:00 UT (Fig. 10)
Plasma motions from the southern region of the erupted filament towards the southern boundary of the CH and from the north-east of the filament towards the western boundary of the CH.	August 31, 23:00 UT–September 3, 16:00 UT (Fig. 10)
Disappearance of the CH and DR.	September, 1 02:00 UT–September 4, 08:00 UT (Fig. 10)

Additionally, in order to study the perturbed region between the filament channel and the CH boundary, we selected a sector ( $15^\circ \times 12^\circ$ ) from this region based on the SDO/AIA 193 Å images and divided it into 11 segments or cuts, parallel to the solar equator (Fig. 5a). We have used the method, similar to that reported by McIntosh et al. (2011), Shen, Liu & Su (2012), Verwichte et al. (2013) and Ma et al. (2014). We elaborated the time evolution map of each cut during 10 h, starting at 00:00 UT on August 8, which is the preceding period to the CH disappearance. Fig. 5(b) shows one part of this map that reveals the CH evolution and its disappearance related to the arrived plasma. Generally, all segments of this map show the filament plasma disturbances and wavy behaviour of the longitudinally moving plasma from the filament channel towards the CH boundary (clearly observed from 07:00 to 07:42 UT, Fig. 5c). We believe that they are MHD waves involved in the magnetic reconnection process and are related to the filament plasma instabilities. We made the same analysis of SDO/AIA 304, 171 and 211 Å images and obtained similar results observed in the 304 and 171 Å images, but to a lesser extent in the 211 Å images, which depicts the specific low coronal region where MHD waves are propagated. Fig. 6 shows the time evolution of cuts 4, 6 and 8 in the 171 Å images, and Fig. 6(d) shows the wave-like dynamics of the moving plasma (with a period of about 15 min) through a small region of cut 8 during the period of 07:30–08:00 UT. Moreover, based on the time evolution map of cut 4 (in the 193 Å images, Fig. 7), we estimated

the average speed of propagation (Shen et al. 2012, have reported a similar method for the filament eruption) of  $\sim 17.53 \text{ km s}^{-1}$  of the longitudinally moving plasma from the filament channel towards CH, within the time range of ~06:20–06:40 UT.

### 3.3 Events of August 31, 2012

The next Carrington rotation observations show the reformed filament close to the East limb with the CH and the DR at similar positions. At ~17:00 UT, August 31, the prominence expansion started, at 19:30 UT the prominence twisted significantly and then at ~19:45 UT the whole prominence started erupting slowly. This eruption accelerated when its southern footpoint reconnected with the nearest AR 11563. Then, a long duration associated C8.4 flare and type II radio burst and the subsequent Halo CME3 started almost simultaneously at 20:10 UT (Fig. 9 and Table 1). At ~20:26 UT, we observed the evacuated prominence material. After ~25 min, the post-flare loops formed that extended to the AR 1162 (Fig. 10). In order to study this eruption in detail, we selected a sector ( $110^\circ < \theta < 140^\circ$  and  $0.4R_S < R < 1.45R_S$ , Fig. 8a) from the SDO/AIA 193 Å images, made an  $R - \theta$  map (Fig. 8b), chose a cut at the angular position  $\theta = 121.96^\circ$  (white line, Fig. 8b), which corresponds to the centre of the prominence body during its eruption, and finally obtained the corresponding time evolution map (Fig. 8c). A similar method has been reported by McIntosh et al. (2011). This map allowed



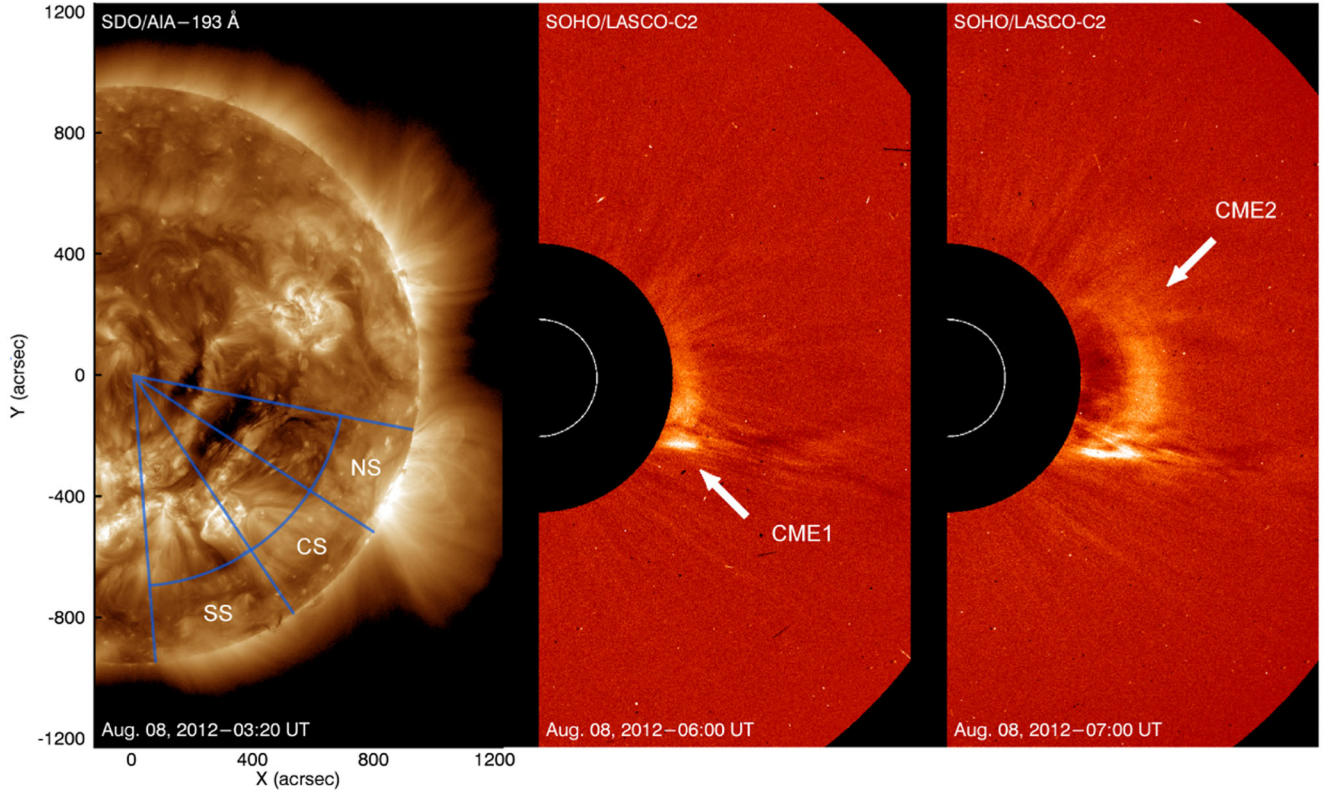


**Figure 2.** Left: SDO/AIA 193 Å image of 2012 August 8, 03:20 UT. The red lines delimit the three sections of the filament: north (NS), central (CS) and south (SS). The position angle of each section is  $PA_{NS} \sim 254^\circ$ ,  $PA_{CS} \sim 225^\circ$  and  $PA_{SS} \sim 210^\circ$ . Right: CME1 ( $PA \sim 255^\circ$ ,  $W \sim 20^\circ$ ) and CME2 ( $PA \sim 275^\circ$ ,  $W \sim 60^\circ$ ), respectively; we estimated these values of width based on SOHO/LASCO-C2 images.

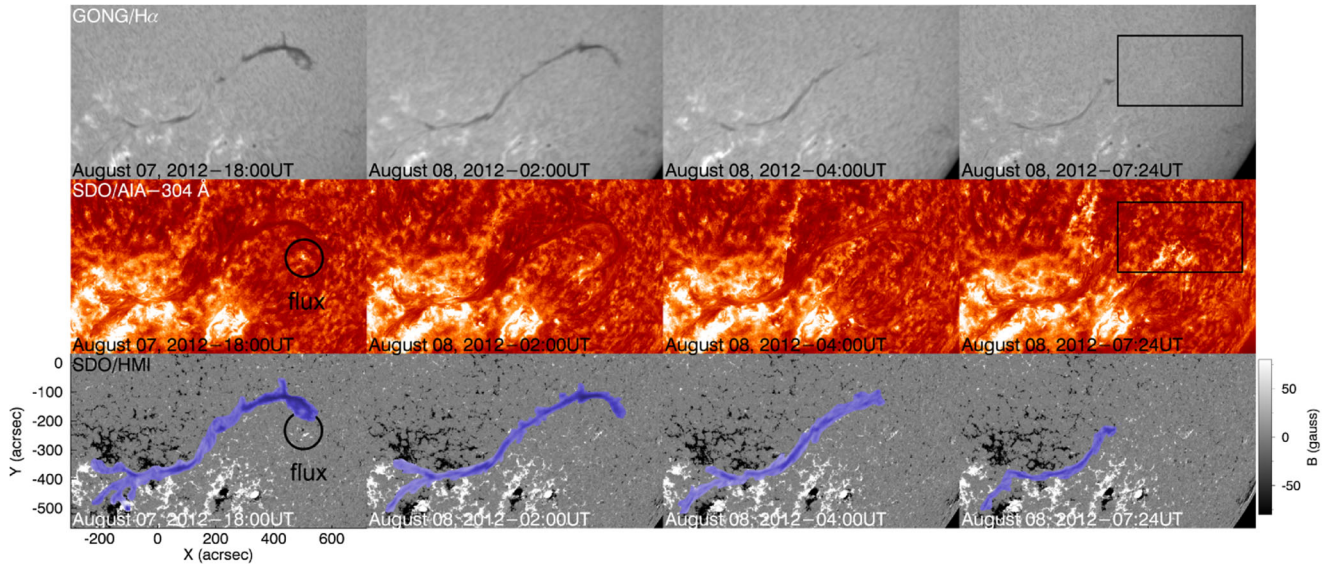


**Figure 3.** GONG/H $\alpha$  and SDO/AIA 304 Å ( $T = 5 \times 10^4$  K) images and SDO/HMI magnetograms for 2012 August 7–8. The magnetogram scale is displayed to the right side of the figure. The black rectangles show the DBDs of a part of CS and the whole NS, and the black circle shows the magnetic flux, which disappeared almost simultaneously with DBDs.

us to estimate the velocity and acceleration of the prominence plasma using the adjustment  $h = A(\log(\cosh(Bt + C))) + Dt + E$  of the eruption trajectory and obtain its temporal derivatives (Sheeley, Warren & Wang 2007; Alissandrakis et al. 2013). These results are shown in Figs 8(d) and (e). We applied this method to

each of the SDO/AIA EUV channel observations and obtained very similar results. The prominence plasma accelerated from  $\sim 19:30$  UT, in  $\sim 25$  min its propagating speed reached  $V \sim 700 \text{ km s}^{-1}$  (Fig. 8d) and was followed by the Halo CME3 (reported by CACTus as a semi-Halo), with  $V_{\text{linear}} \sim 1442 \text{ km s}^{-1}$  (SOHO/LASCO-



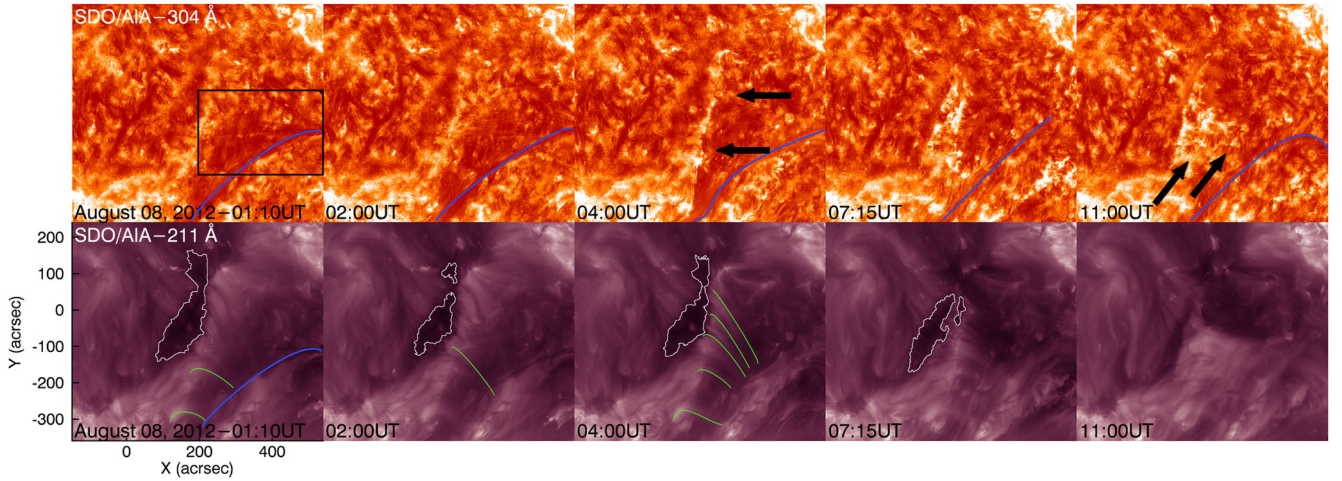


**Figure 4.** SDO/AIA 304 Å ( $T = 5 \times 10^4$  K) and SDO/AIA 211 Å ( $T = 2 \times 10^6$  K) images. CH boundaries are enhanced with white colour. Some loops between the filament (blue colour) and CH surroundings are enhanced with green colour. The black rectangle enclosed the CS and NS, as well as the surrounding region of the filament, related with the possible magnetic reconnection between the filament footpoints and the CH boundary. With the black arrows we indicate the plasma that is moving towards the CH.

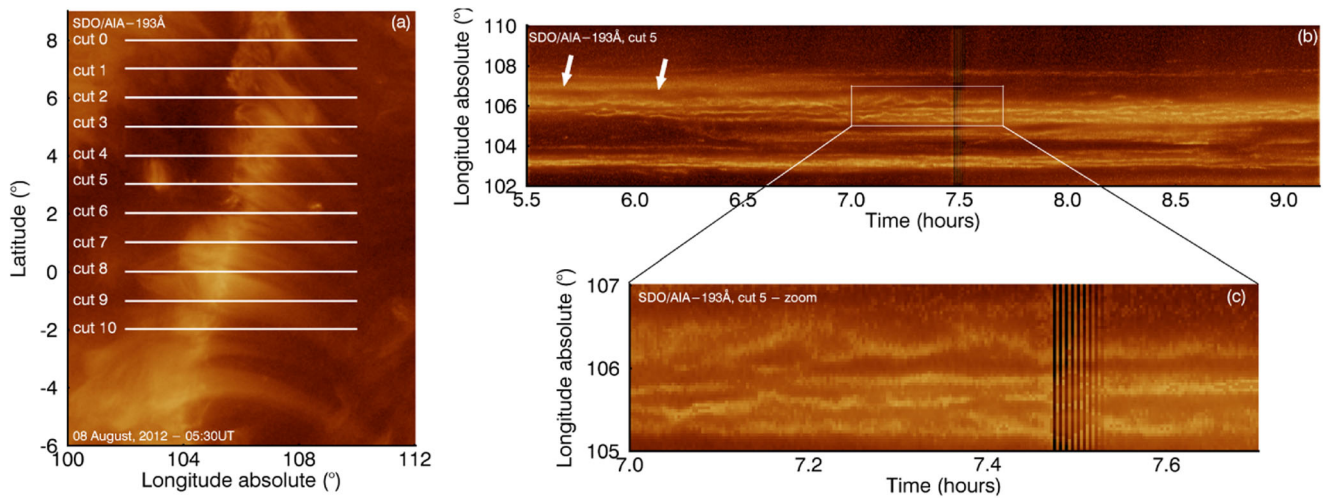


**Figure 5.** (a) The sector of  $15^\circ \times 12^\circ$  of the SDO/AIA 193 Å ( $T = 1 \times 10^6$  K) image for 2012 August 8, 05:30 UT, which includes CH and its surroundings. Each of the eleven white lines corresponds to a segment or a cut (of  $\sim 8^\circ$  longitudinal  $\times$  0.6 arcsec (or 1 pixel) latitudinal extensions), parallel to the solar equator. (b) The time evolution map of cut 5 for the period of 05:30–09:10 UT. The dark region corresponds to the CH, and the white arrows indicate the direction of the plasma propagation. (c) Zoom of the white box from (b) shows the oscillatory behaviour of the moving plasma during the period of 07:00–07:42 UT.

C2:  $2.0 R_S - 6.0 R_S$ ),  $V_{\text{medium}} \sim 520 \text{ km s}^{-1}$  and  $V_{\text{max}} \sim 892 \text{ km s}^{-1}$  (STEREO-B/SECCHI-COR2:  $1.1 R_S - 3.0 R_S$ ). These results indicate an additional CME acceleration starting at a height of  $3 R_S$ . Fig. 9 shows the  $R - \theta$  map of this sector based on the STEREO-B/EUVI 304 Å images that include the twisted prominence with a possible X-point of reconnection (white arrow) and the associated Halo CME3 (STEREO-B/ SECCHI-COR1).

Moreover, after the eruption we observed strong perturbations of the region between the filament channel and the CH where multiple coronal loops formed (Fig. 10). Several hot loops formed first, after the prominence eruption, which was accompanied by the C8.4 flare and type II radio burst (August 31, 22:30 UT, Fig. 10), whereas some other cooler loops formed later,  $\sim 24$  h after CME3 (green colour, Fig. 10). This loop formation was accompanied by the evacuated

filament plasma motions from the southern region of the erupted filament towards the southern boundary of the CH and from the northeast of the filament towards the western boundary of the CH (black arrows, Fig. 10). About 6 h after the eruption, the additional plasma arrived at the northern part of the CH from the southeast region of the erupted filament (white arrows, Fig. 10). As a result, the CH started to fade slowly from all directions and disappeared completely  $\sim 3.5$  d after the filament eruption (Fig. 10). From September 4, the whole filament with a sigmoid form was observed again in the  $H\alpha$  images.

During the post-filament eruption and post-CME3 processes, we observed the waves propagating longitudinally from the filament channel towards the western boundary of the CH. Applying the same method, which we had previously used for the post-filament

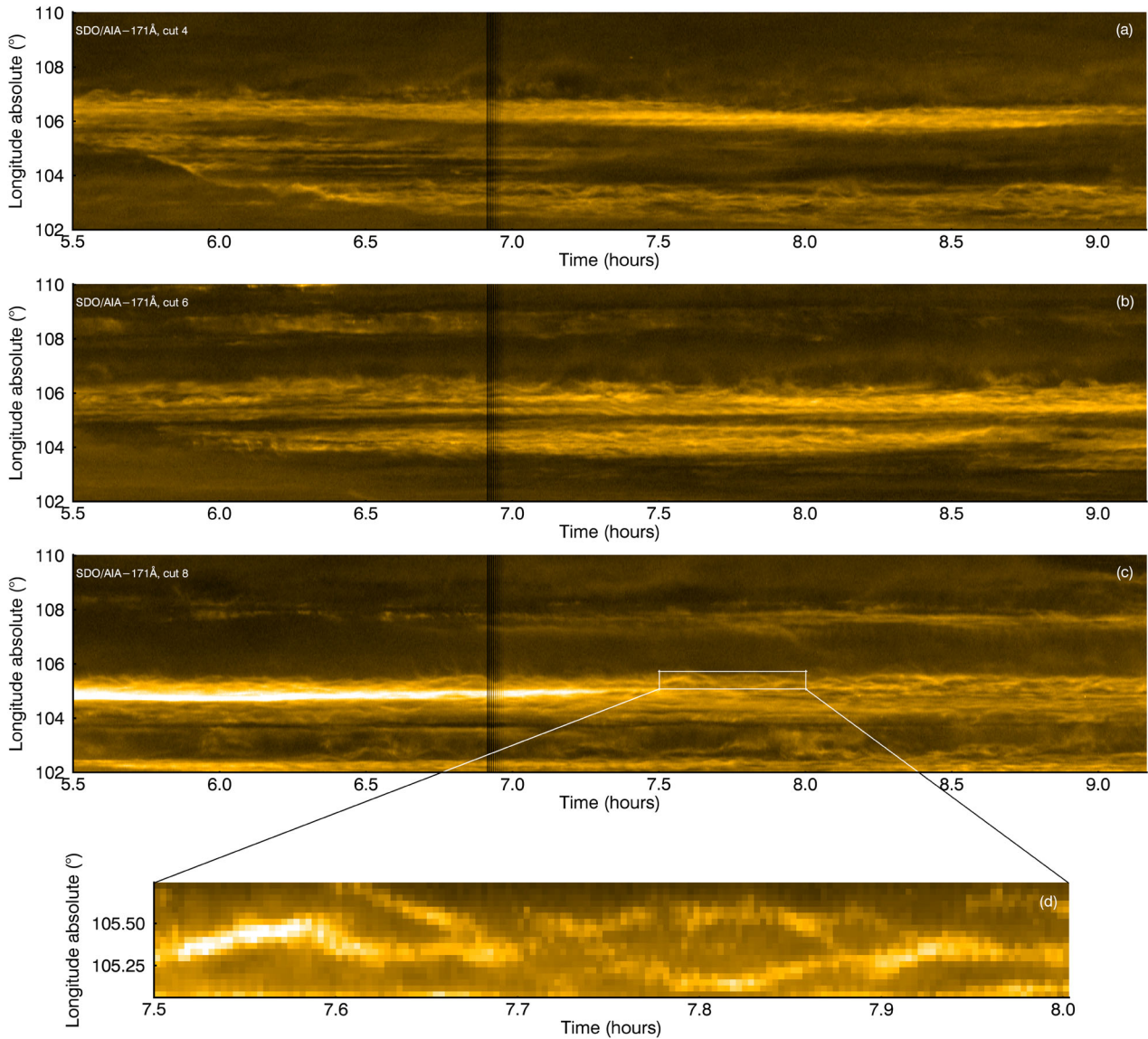


**Figure 6.** (a–c) The time evolution map of cuts 4, 6 and 8 (from Fig. 5a) based on the SDO/AIA 171 Å ( $T = 6 \times 10^5$  K) images for 2012 August 8, 05:30–09:10 UT. (d) Zoom of the white box from (a) that shows the wavy behaviour of the perturbed region between the filament channel and the CH boundary from 07:30 to 08:00 UT.

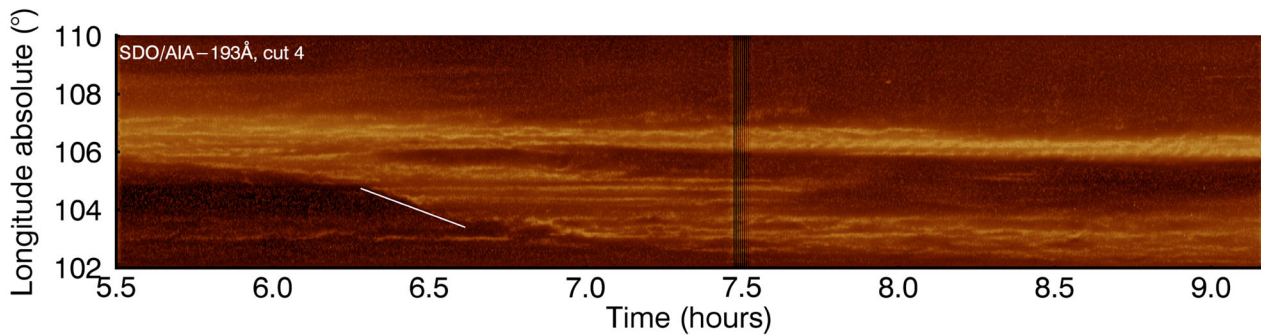


**Figure 7.** The time evolution map of cut 4 (from Fig. 5a) based on the SDO/AIA 193 Å images for 2012 August 8. The white line indicates a uniform plasma motion that we consider as a proxy for estimating the average speed of propagation ( $\sim 17.53$  km s $^{-1}$ ).



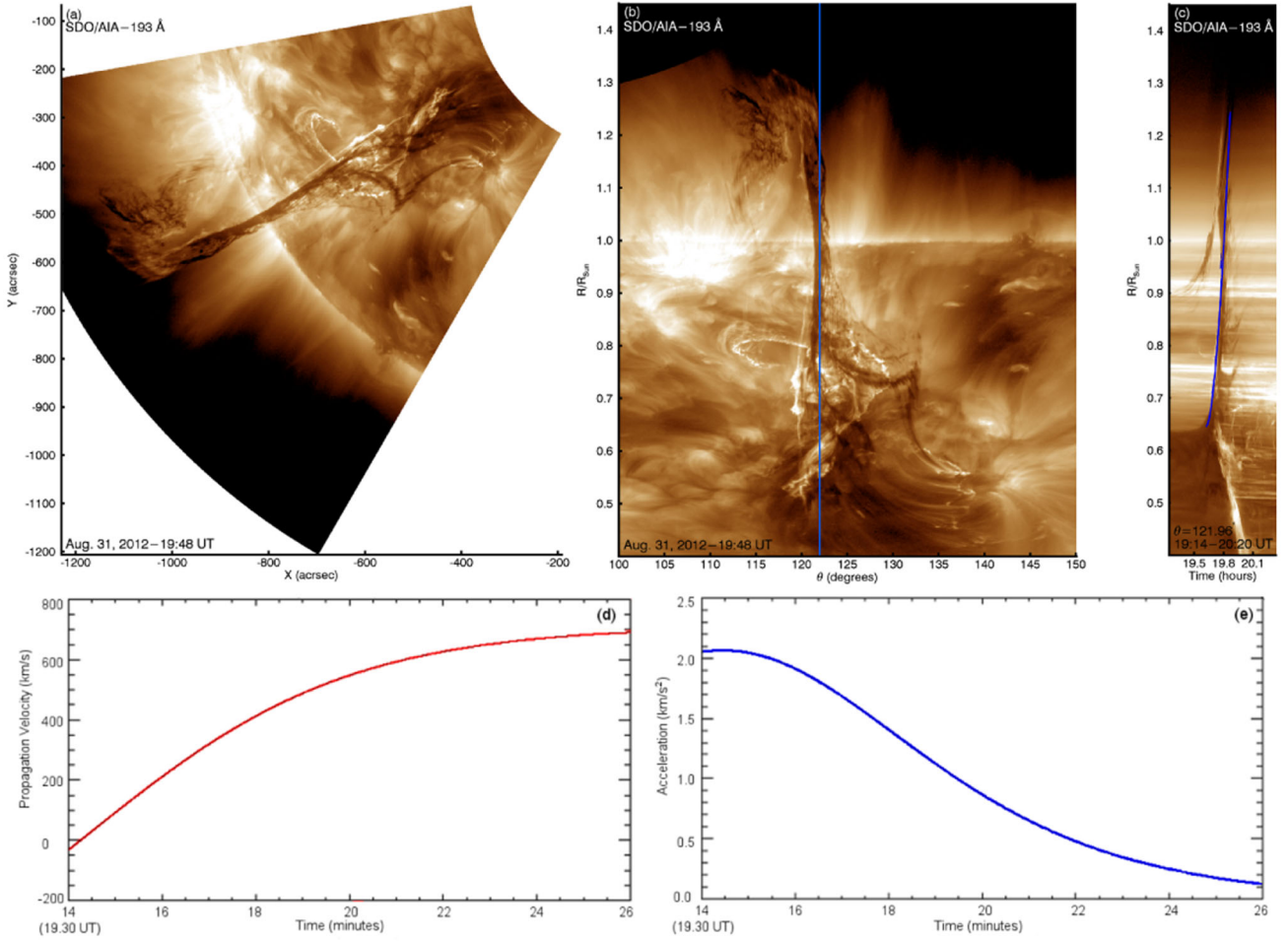


**Figure 8.** (a) The sector ( $110^\circ < \theta < 140^\circ$  and  $0.4 R_S < R < 1.45 R_S$ ) of the SDO/AIA 193 Å image for August 31, 19:48 UT. (b)  $R - \theta$  map of this sector; the blue line corresponds to the cut at the angular position  $\theta = 121.96^\circ$ . (c) Temporal evolution of this cut; the blue line corresponds to the fit of the filament eruption trajectory. (d–e) The filament plasma speed and acceleration calculated from the fit.

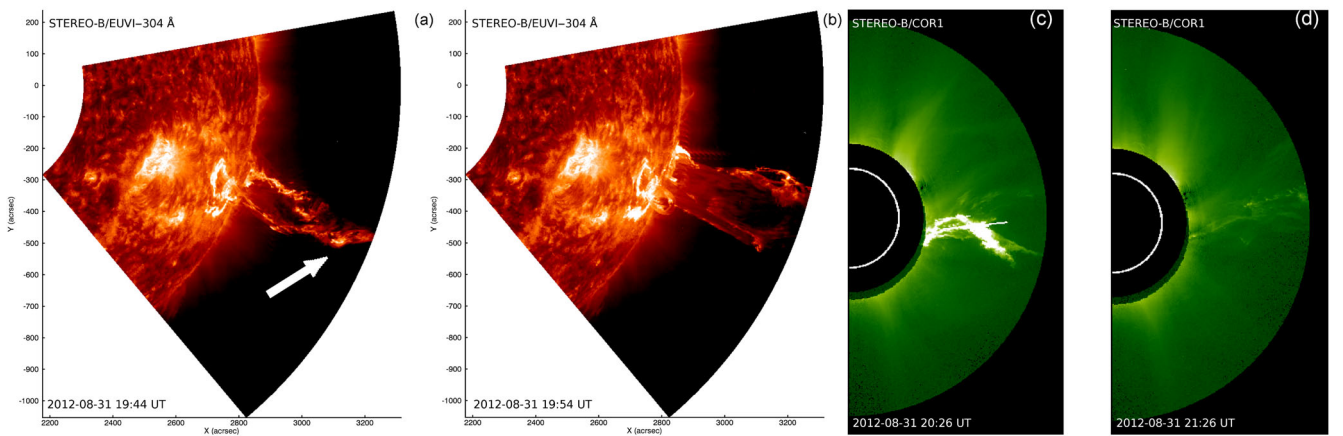


**Figure 9.** (a and b) Sectors of STEREO-B/EUVI 304 Å images for August 31, 19:49 and 19:54 UT. The twisted filament eruption is clearly observed (white arrow). (c and d) STEREO-B/COR1 images of the Halo CME3, observed at 20:26 and 21:26 UT.

eruption waves of August 8, we analysed several cuts through the perturbed region and obtained a similar result of the possible MHD waves (Fig. 11). We also observed the disappearance of several bright points, associated with the small magnetic dipoles, near and

inside the CH that accompanied this process. Moreover, SDO/HMI magnetograms show the magnetic diffusion at the southern part of the perturbed region that started slowly after the wave/turbulence dissipation and onset of the CH fading.



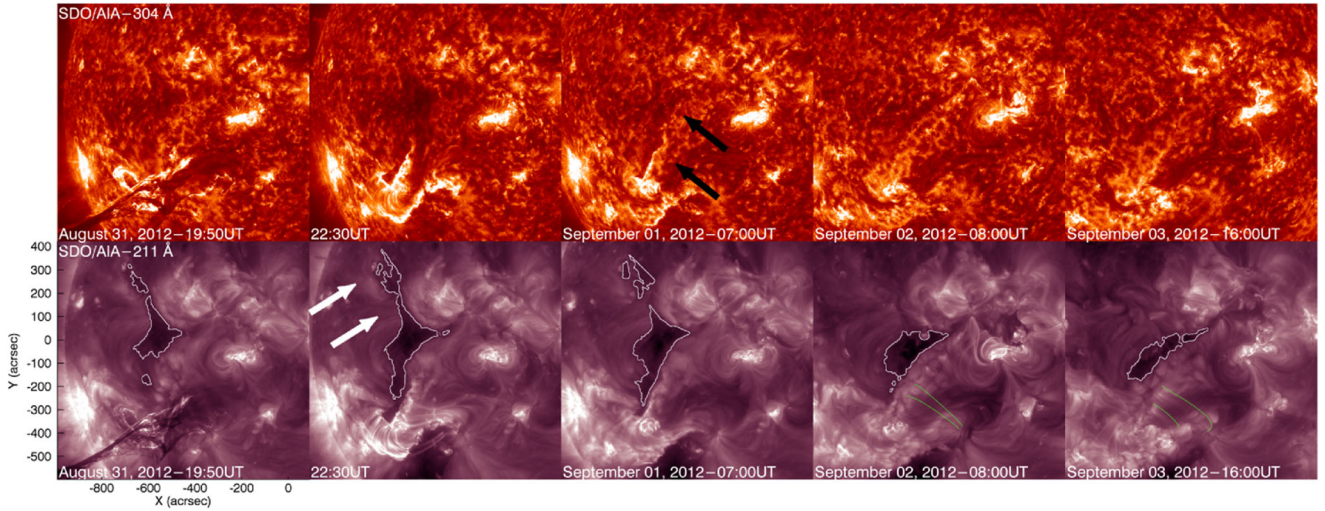


**Figure 10.** SDO/AIA 304 Å and SDO/AIA 211 Å images. The CH boundaries are enhanced with white colour and several cool loops near to the CH with green colour. The black arrows indicate the plasma that is moving towards the southern part of the CH and white arrows indicate the plasma that is moving towards the northern part of the CH.

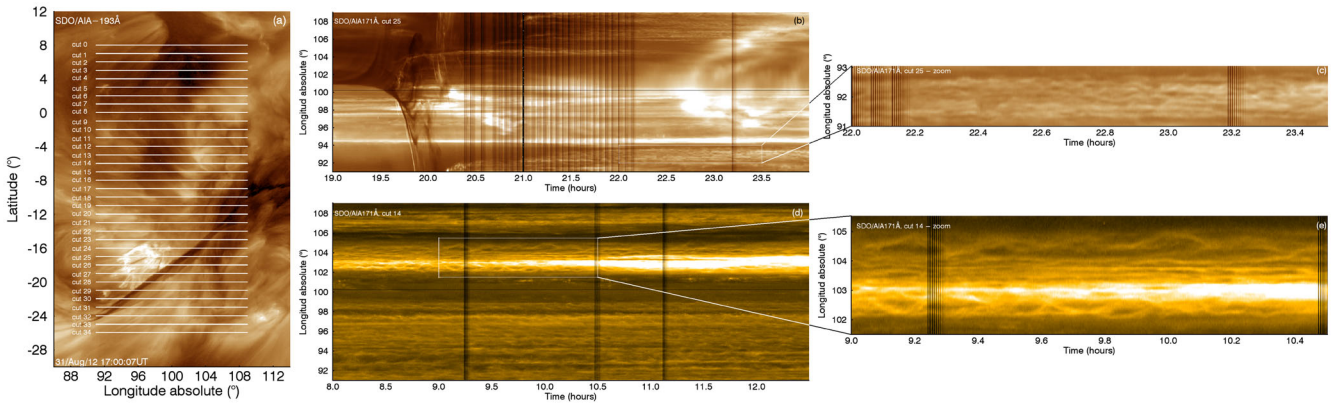


**Figure 11.** (a) The sector of  $42^\circ \times 28^\circ$  of the SDO/AIA 193 Å image for 2012 August 31, 22:47 UT, which includes the CH, the filament and their surroundings. Each of the white lines corresponds to a segment or cut [of  $\sim 18^\circ$  longitudinal  $\times$  0.6 arcsec (or 1 pixel) latitudinal extensions], parallel to the solar equator. (b) The time evolution map of cut 21 for the period of 19:00–23:59 UT, August 31, based on SDO/AIA 193 Å images. The white arrow indicates the filament eruption. (c) Zoom of the white box from (b) shows wavy behaviour of the moving plasma during the period of 21:00–22:30 UT. (d) The time evolution map of cut 10 for the period of 08:00–12:30 UT, September 1, based on SDO/AIA 171 Å images. (e) Zoom of the white box from (d) shows the wavy behaviour of the moving plasma during the period of 10:30–12:15 UT.

#### 4 CONCLUSIONS

We have presented the results of a detailed study of the evolution of equatorial CH and DR related to the nearby large equatorial quiescent filament/prominence eruptions and the associated CMEs. The filament and the CH are separated by  $\sim 15^\circ$ , which is a critical distance for the interaction between them (Taliashvili et al. 2009; Panasenco et al. 2011; Gutiérrez et al. 2013). This filament is characterized by the different evolutionary stages that we have discussed previously (Taliashvili et al. 2014). In this study, we focused on the filament partial eruptions occurred on August 8 and the filament complete eruption occurred on August 31.

The first instability was started by increasing disturbances of the filament body anticipated by the emergence of several small magnetic fluxes close to the filament footpoints. Then, the filament plasma moved from its southern to the northern footpoint and vice versa accompanied by the perturbations of the region between the

filament and CH that includes the DR. In this perturbed region, several fluxes disappeared and the post-filament eruption EUV loop formed, followed by the plasma motions from the filament channel towards the CH boundary. This moving plasma is related to one part of the filament plasma, which is not involved in the filament partial eruptions of August 8. These processes are indicators of the possible magnetic reconnection involving the filament footpoints and CH boundaries (Madjarska et al. 2004; Gutiérrez et al. 2013). On the other hand, a cadence of the possible magnetic photospheric reconnection could have occurred as we observe a strong turbulence of the filament body, the flux cancellation close to the filament footpoints, the filament partial eruptions and the associated two CMEs. It is well known that the relation between the prominence dynamic eruptions and CMEs is due to magnetic reconnection, frequently anticipated by the emergence of a new magnetic flux at one of the footpoints of the filament (Mouradian et al. 1987), while

the energy is transported by waves along the flux tubes in the prominence feet from the pivot point (Mouradian & Soru-Escut 1989). Photospheric motions at footpoints as well as turbulent motions within different sections of the filament probably induce kink instability and a partial eruption of the filament. At the next Carrington rotation, a significant twist was added by the reconnection to the rising flux in the course of an eruption (e.g. Qiu et al. 2007). Flux ropes could reconnect and merged prior to an eruption, thereby adding up their respective twists (e.g. Pevtsov, Canfield & Zirin 1996; Canfield & Reardon 1998; Schmieder et al. 2004). This was especially well observed on the August 31 event. Our observations display the twisted prominence body, anticipated by strong disturbances and the prominence expansion, started just before its complete and slow eruption, leading probably to the torus instability. The flux rope that is progressively formed by photospheric reconnection and successively by flux cancellation approaches a critical point of the equilibrium curve driven by a constant increase of the twist and/or by changing the magnetic flux below/above the flux rope, removes the overlying arcades by coronal reconnection and erupts by developed torus instability (Kliem & Török 2006; Aulanier et al. 2010, and their references; Schmieder et al. 2013, review). This slow filament eruption was accelerated when its southern footpoint reconnected with the nearest AR and was followed by a long duration flare, type II radio burst and the subsequent Halo CME. The post-filament eruption and post-CME evolution for both cases of August 8 and 31 were characterized by strong perturbations of the region between the filament channel and the CH. In this perturbed region, after the filament eruption and CME, several EUV loops formed followed by the longitudinally moving plasma and MHD waves. The moving plasma and MHD waves propagating away from the possible reconnection region reached DR/CH and induced the onset of their fading. Finally, we observed the magnetic diffusion that started after the wave/turbulence dissipation and the onset of CH/DR fading, as well as a magnetic realignment of the region that enclosed them. The magnetic reconnection and magnetic diffusion associated with both cases of filament eruption control the evolution of the CH area (Gutiérrez et al. 2013; Hiremath & Hegde 2013).

Our observations indicate a close connection of disorganized motions in the filament body and reconnection. The turbulence and oscillations and waves are related. For instance, in Lazarian (2016), it is described how the oppositely moving packets of Alfvénic waves generate turbulence. If a wave is propagating in one direction, a reflected wave is expected in the other direction. Even in unrealistically homogeneous plasmas the reflection is possible due to the parametric instability. The post-filament eruption and post-CME longitudinally propagated waves that we observed are probably the reflected Alfvén waves associated with these processes. Alfvén waves that propagate along a flux tube with a radially varying Alfvén-speed undergo partial reflection back towards the Sun (Heinemann & Olbert 1980; Velli 1993). The existence of counter-propagating wave packets, even if only a small fraction of the energy is coming back, allows a non-linear MHD turbulent cascade to develop. In the case of the balanced cascade, i.e. when the energy flows are the same in opposite directions, the theory is most developed (Iroshnikov 1963; Kraichnan 1965; Dobrowolny, Mangeney & Veltri 1980; Velli, Grappin & Mangeney 1989; Goldreich & Sridhar 1995; Lazarian & Vishniac 1999; Cho & Vishniac 2000; Maron & Goldreich 2001; Cho & Lazarian 2002; Cho, Lazarian & Vishniac 2002). For the imbalanced cascade, i.e. when the energy flux in one direction exceeds the energy flux in the opposite direction; the imbalanced cascade emerges (see Beresnyak &

Lazarian 2008, 2009). Both balanced turbulence and imbalanced turbulence induce magnetic field wandering that induces fast magnetic reconnection (see Lazarian et al. 2015, for a review). On the whole, from the point of view of the theory, we expect to have a case of imbalanced MHD turbulence (see Beresnyak & Lazarian 2007, 2009), which can vary in a large range according to Goldreich & Sridhar (1995). Nevertheless, this type of turbulence is expected to induce magnetic field line stochastic motions (see Eyink et al. 2011) and consequently induce magnetic reconnection. A cadence of the possible magnetic reconnection takes place primarily by the filament body turbulence, which is in agreement with the turbulent reconnection theory (Lazarian & Vishniac 1999). It is also important to point out that the plasma motions and CH disappearance were faster after the partial filament eruptions of August 8, which lasted just about 12 h, whereas after the whole filament eruption of August 31, the process lasted almost 3.5 d. We consider this difference to be related to the stronger filament plasma turbulence involved in the pre-filament eruption and the magnetic reconnection processes related to the filament partial eruptions as well as to the perturbed region of shared and the turbulent post-eruption/CME plasma. The turbulence can be pre-existing but is also self-generated by the reconnection process; the turbulence is spontaneous, with available energy released by a rich array of instabilities, such as kink instability of twisted flux tubes in the solar corona as well as hydrodynamic instabilities associated with the outflow (Lazarian et al. 2015). While our study cannot quantitatively check the prediction of the turbulent reconnection theory, we definitely observe a very close relation between magnetic reconnection and the generation of turbulence and MHD waves, which is consistent with what is expected in turbulent reconnection.

General magnetic reconfiguration, associated with the post-eruption evolution of these long-lived prominence and the CH, which is characterized by very stable magnetic fields, also involved some ARs, located very close to the filament southern footpoint, especially, the associated C8.4 flare and type II radio burst of August 31, which started after the prominence eruption and allowed the input of the additional energy released and the destabilization of the whole region. The destabilization of the reconnecting region—which entails bursts of reconnection—is part of one of the predictions of the theory of turbulent reconnection (Lazarian et al. 2009). Another prediction related to the reconnection layer was first tested by Ciaravella & Raymond (2008), and an improved analysis was presented in Lazarian et al. (2015). Other papers explored the similarity of magnetic reconnection in turbulent MHD simulations and in the solar wind (Lalescu et al. 2015). The propagation of the reconnection front and triggering of reconnection by turbulence induced in other regions (see Sych et al. 2009) are the problems that require further detailed study.

The processes that we observed can also be linked to the problem of the heating of solar corona, which is affected by the combination of wave/turbulence dissipation and magnetic reconnection (Cranmer et al. 2015). However, the evolution of magnetic reconnection led by the turbulence requires further analysis. To provide a study of the associated physics and test the theory, complex and detailed magnetic observations are required, which in turn can more clearly reveal the process of the evolution of coronal and interplanetary magnetic fields.

## ACKNOWLEDGEMENTS

We are grateful to the Solar TERrestrial RELations Observatory, SOLar (STEREO) and Heliospheric Observatory (SOHO), Solar



Dynamics Observatory (SDO), Paris Observatory (PO) and Global High Resolution H-alpha Network for open access to their data sets. SDO is a mission for NASA's Living with a star (LWS) programme. Large Angle Spectroscopic CORonagraph (LASCO) is part of SOHO, SOHO is a project of international cooperation between European Space Agency (ESA) and National Aeronautics and Space Administration, Washington, D.C. (NASA). The LASCO CME catalog is generated and maintained at the Coordinated Data Analysis Workshop (CDAW) Data Center by NASA and The Catholic University of America in cooperation with the Naval Research Laboratory. The STEREO mission is supported by NASA, The Particle Physics and Astronomy Research Council (PPARC, United Kingdom, UK), Deutsche Zentrum für Luft- und Raumfahrt e. V. (DLR, Germany), Centre national d'études spatiales (CNES, France), and United States Air Force (USAF, United States of America, USA). The Sun Earth Connection Coronal and Heliospheric Investigation (SECCHI) data used here were produced by an international consortium of the Naval Research Laboratory (USA), Lockheed Martin Solar and Astrophysics Lab (USA), NASA Goddard Space Flight Center (USA), Rutherford Appleton Laboratory (UK), University of Birmingham (UK), Max-Planck-Institut für Solar System Research (Germany), Centre Spatial de Liège (Belgium), Institut d'Optique Théorique et Appliqué (France), Institut d'Astrophysique Spatiale (France). The "COR1 Preliminary Events List" was generated by O. C. St. Cyr prior to September 2007, and is being maintained now by Hong Xie. Wilcox Solar Observatory data used in this study was obtained via the web site <http://wso.stanford.edu> at 2016:09:05\_21:00:58 PDT courtesy of J.T. Hoeksema. The Wilcox Solar Observatory is currently supported by NASA. This work is supported by NSF grant AST 1212096 and NASA grant NNX14AJ53G to Alexandre Lazarian. This study was performed as a partial requirement for the PhD Degree of Sciences at the University of Costa Rica to Heidy Gutiérrez. Special thanks are owed to anonymous referees for constructive comments that helped to improve the quality of the paper.

## REFERENCES

- Alissandrakis C. E., Kochanov A. A., Patsourakos S., Altyntsev A. T., Lesovoi S. V., Lesovoya N. N., 2013, *PASJ*, 65
- Atrill G., Nakwacki M. S., Harra L. K., van Driel-Gesztelyi L., Mandrini C. H., Dasso S., Wang J., 2006, *Sol. Phys.*, 238, 117
- Aulanier G., Török T., Démoulin P., DeLuca E. E., 2010, *ApJ*, 708, 314
- Beresnyak A., 2013, *ApJ*, 767, L39
- Beresnyak A., Lazarian A., 2007, in Haverkorn M., Goss W. M., eds, *ASP Conf. Ser. Vol. 365, SINS – Small Ionized and Neutral Structures in the Diffuse Interstellar Medium*. Astron. Soc. Pac., San Francisco, p. 139
- Beresnyak A., Lazarian A., 2008, *ApJ*, 682, 1070
- Beresnyak A., Lazarian A., 2009, *ApJ*, 702, 1190
- Brandenburg A., Lazarian A., 2013, *Space Sci. Rev.*, 178, 163
- Bravo S., 1995, *Sol. Phys.*, 161, 57
- Brueckner G. E. et al., 1995, *Sol. Phys.*, 162, 357
- Canfield R. C., Reardon K. P., 1998, *Sol. Phys.*, 182, 145
- Cho J., Lazarian A., 2002, *Phys. Rev. Lett.*, 88, 245001
- Cho J., Vishniac E. T., 2000, *ApJ*, 539, 273
- Cho J., Lazarian A., Vishniac E. T., 2002, *ApJ*, 564, 291
- Ciaravella A., Raymond J. C., 2008, *ApJ*, 686, 1372
- Cranmer S. R., 2002, in Wilson A., ed, *ESA SP-508: From Solar Min to Max: Half a Solar Cycle with SOHO*. ESA, Noordwijk, p. 361
- Cranmer S. R., van Ballegoijen A. A., 2005, *ApJS*, 156, 265
- Cranmer S. R., Asgari-Targhi M., Miralles M. P., Raymond J. C., Strachan L., Tian H., Woolsey L. N., 2015, *Phil. Trans. R. Soc. A*, 373, 20140148
- de Toma G., Holzer T. E., Burkepile J. T., Gilbert H. R., 2005, *ApJ*, 621, 1109
- Dobrowolny M., Mangeney A., Veltri P., 1980, *Phys. Rev. Lett.*, 45, 144
- Domingo V., Fleck B., Poland A. I., 1995, *Sol. Phys.*, 162, 1
- Duvall T. L. Jr, Wilcox J. M., Svalgaard L., Scherrer P. H., McIntosh P. S., 1977, *Sol. Phys.*, 55, 63
- Eyink G. L., Lazarian A., Vishniac E. T., 2011, *ApJ*, 743, 51
- Farmer A. J., Goldreich P., 2004, *ApJ*, 604, 671
- Gibson S. E., Low B. C., 2000, *J. Geophys. Res.*, 105, 18187
- Goldreich P., Sridhar S., 1995, *ApJ*, 438, 763
- Gopalswamy N., Mikić Z., Maia D., Alexander D., Cremades H., Kaufmann P., Tripathi D., Wang Y.-M., 2006, *Space Sci. Rev.*, 123, 303
- Gutiérrez H., Taliashvili L., Mouradian Z., 2013, *Adv. Space Res.*, 51, 1824
- Heinemann M., Olbert S., 1980, *J. Geophys. Res.*, 85, 1311
- Hiremath K. M., Hegde M., 2013, *ApJ*, 763, 137
- Hollweg J. V., 1981, *Sol. Phys.*, 70, 25
- Howard R. A. et al., 2008, *Space Sci. Rev.*, 136, 67
- Hudson H. S., Acton L. W., Freeland S. L., 1996, *ApJ*, 470, 629
- Iroshnikov P. S., 1963, *AZh*, 40, 742
- Jiang Y., Yang L., Li K., Shen Y., 2007, *ApJ*, 667, L105
- Kahler S. W., Hudson H. S., 2001, *J. Geophys. Res.*, 106, 29239
- Kaiser M. L., 2005, *Adv. Space Res.*, 36, 1483
- Kliem B., Török T., 2006, *Phys. Rev. Lett.*, 96, 255002
- Kowal G., Lazarian A., Vishniac E. T., Otmianowska-Mazur K., 2009, *ApJ*, 700, 63
- Kraichnan R. H., 1965, *Phys. Fluids*, 8, 1385
- Krieger A. S., Timothy A. F., Roelof E. C., 1973, *Sol. Phys.*, 29, 505
- Krista L. D., Reinard A., 2013, *ApJ*, 762, 91
- Lalescu C. C., Shi Y.-K., Eyink G. L., Drivas T. D., Vishniac E. T., Lazarian A., 2015, *Phys. Rev. Lett.*, 115, 025001
- Lazarian A., 2016, *ApJ*, 833, 131
- Lazarian A., Vishniac E. T., 1999, *ApJ*, 517, 700
- Lazarian A., Vishniac E., Kowal G., 2009, in Pogorelov N. V., Audit E., Colella P., Zank G. P., eds, *ASP Conf. Ser. Vol. 406, Numerical Modeling of Space Plasma Flows: ASTRONUM-2008*. Astron. Soc. Pac., San Francisco, p. 23
- Lazarian A., Eyink G., Vishniac E., Kowal G., 2015, *Phil. Trans. R. Soc. A*, 373, 20140144
- Lemen J. R. et al., 2012, *Sol. Phys.*, 275, 17
- Ma L., Qu Z.-Q., Yan X.-L., Xue Z.-K., 2014, *Res. Astron. Astrophys.*, 14, 1481
- Madjarska M. S., Doyle J. G., van Driel-Gesztelyi L., 2004, *ApJ*, 603, L57
- Maron J., Goldreich P., 2001, *ApJ*, 554, 1175
- McIntosh S. W., de Pontieu B., Carlsson M., Hansteen V., Boerner P., Goossens M., 2011, *Nature*, 475, 477
- Mouradian Z., Soru-Escaut I., 1989, *A&A*, 210, 410
- Mouradian Z., Martres M. J., Soru-Escaut I., 1980, in Moriyama F., Henoux J. C., eds, *Proceedings of the Conference, Japan–France Seminar on Solar Physics*, p. 195
- Mouradian Z., Martres M. J., Soru-Escaut I., 1986, in Poland A. I., ed, *NASA. Goddard Space Flight Center Coronal and Prominence Plasmas*, Vol. 2442. NASA Goddard Space Flight Center, Greenbelt, MD, US, p. 221
- Mouradian Z., Martres M. J., Soru-Escaut I., Gesztelyi L., 1987, *A&A*, 183, 129
- Murawski K., Solov'ev A., Musielak Z. E., Srivastava A. K., Książek J., 2015, *A&A*, 577, A126
- Panasenco O., Martin S., Joshi A. D., Srivastava N., 2011, *J. Atmos. Sol.-Terr. Phys.*, 73, 1129
- Pesnell W. D., Thompson B. J., Chamberlin P. C., 2012, *Sol. Phys.*, 275, 3
- Pevtsov A. A., Canfield R. C., Zirin H., 1996, *ApJ*, 473, 533
- Qiu J., Hu Q., Howard T. A., Yurchyshyn V. B., 2007, *ApJ*, 659, 758
- Raadu M. A., Schmieder B., Mein N., Gesztelyi L., 1988, *A&A*, 197, 289

- Rust D. M., 1983, *Space Sci. Rev.*, 34, 21
- Scherrer P. H., Wilcox J. M., Svalgaard L., Duvall T. L., Jr, Dittmer P. H., Gustafson E. K., 1977, *Sol. Phys.*, 54, 353
- Schmieder B., Mein N., Deng Y., Dumitrache C., Malherbe J.-M., Staiger J., Deluca E. E., 2004, *Sol. Phys.*, 223, 119
- Schmieder B., Démoulin P., Aulanier G., 2013, *Adv. Space Res.*, 51, 1967
- Schou J. et al., 2012, *Sol. Phys.*, 275, 229
- Sheeley N. R. Jr, Warren H. P., Wang Y.-M., 2007, *ApJ*, 671, 926
- Shen Y., Liu Y., Su J., 2012, *ApJ*, 750, 12
- Sych R., Nakariakov V. M., Karlicky M., Anfinogentov S., 2009, *A&A*, 505, 791
- Taliashvili L., Mouradian Z., Páez J., 2009, *Sol. Phys.*, 258, 277
- Taliashvili L., Mouradian Z., Gutiérrez H., 2014, in Schmieder B., Malherbe J.-M., Wu S. T., eds, *IAU Symp. 300, Nature of Prominences and Their Role in Space Weather*. Kluwer, Dordrecht, p. 497
- Tandberg-Hanssen E., 1995, *The Nature of Solar Prominences*, 1 edn. Springer-Science+Business Media, B.V., USA
- Velli M., 1993, *A&A*, 270, 304
- Velli M., Grappin R., Mangeney A., 1989, *Phys. Rev. Lett.*, 63, 1807
- Verwichte E., Van Doorselaere T., Foullon C., White R. S., 2013, *ApJ*, 767, 16
- Waldmeier M., 1975, *Sol. Phys.*, 40, 351
- Wang Y.-M., 2009, *Space Sci. Rev.*, 144, 383
- Yan H., Lazarian A., 2002, *Phys. Rev. Lett.*, 89, 281102

This paper has been typeset from a  $\text{\LaTeX}$  file prepared by the author.